ChemComm

COMMUNICATION

View Article Online
View Journal | View Issue

Cite this: *Chem. Commun.*, 2024, **60**, 2520

Received 1st January 2024,
Accepted 2nd February 2024

DOI: 10.1039/d4cc00001c

rsc.li/chemcomm

Electrogenerated chemiluminescence imaging of plasmon-induced electrochemical reactions at single nanocatalysts†

Qian-Qian Tao,‡[a] Cong-Hui Xu,‡[b] Wei Zhao, *[b] Hong-Yuan Chen[a] and Jing-Juan Xu *[a]

This study explores plasmon-induced electrochemical reactions on single nanoparticles using electrogenerated chemiluminescence microscopy (ECLM). Under laser irradiation, real-time screening showed lower plasmon-induced reaction efficiency for bimetallic Au@Pt nanoparticles compared to monometallic Au nanoparticles. ECLM offers a high-throughput imaging and precise quantitative approach for analyzing photo-electrochemical conversion at single nanoparticle level, valuable for both theoretical exploration and optimization of plasmonic nanocatalysts.

Noble metal nanoparticles, such as Au and Pt, exhibit exceptional catalytic activity, rendering them highly promising materials in the realms of energy conversion and storage. Recognized as plasmonic nanocatalysts, they possess a distinctive optical property known as surface plasmon resonance (SPR).[1–3] The localized SPR excitation initiates a collective oscillation of conduction electrons within the nanostructures. Following SPR excitation, the free electrons rapidly dephase, resulting in the generation of energetic hot electrons and holes. These chemically active species can induce chemical reactions under mild conditions.[4,5] Substantial investigations into hot carriers within plasmonic structures consistently reveal that hot electrons can act as triggers or facilitators in chemical reactions,[2,6–8] while hot holes can enhance the oxidation of adjacent molecules, thereby accelerating the reaction rate.[9,10]

In addition to photocatalytic investigations, plasmon-enhanced electrocatalysis has garnered increasing attention.[11–15] In 2017, Xia and colleagues demonstrated accelerated electrochemical reactions on gold nanoparticles, attributing enhanced electrocatalysis to hot charge carriers generated during plasmon decay.[16] Subsequently, Pensa *et al.* conducted a spectral screening study of hot holes on single gold nanoparticles, identifying three mechanisms contributing to electro-polymerization: enhanced near field, increased metal–liquid interface temperature, and excited electron–hole pairs, with hot carriers as the primary energy reduction contributor.[17]

In the study of photocatalysis and plasmon-enhanced electrocatalysis, a range of electrochemical and optical techniques have been employed, including dark-field microscopy,[17,18] scanning electrochemical microscopy (SECM),[19] and single molecule fluorescence (SMF).[20,21] In recent years, electrogenerated chemiluminescence microscopy (ECLM) has emerged as an important optical-electrochemical imaging technique.[22–25] ECLM leverages electrochemically generated photons to elucidate the electron-transfer process. This approach can capture and analyze electrochemical responses from numerous nanoparticles concurrently. Compared to SMF and SECM with high spatial resolution, the main advantage of ECLM is the high temporal resolution, which allows real-time imaging of electrocatalytic and photocatalytic reactions at individual nanoparticles.

This study introduces an innovative method for electrochemical mapping of hot carrier-assisted electrocatalysis at the single nanoparticle level using ECLM (Fig. 1a). Au nanoparticles (NPs) and Au@Pt core–shell NPs were synthesized for the investigation, leveraging the well-known superior plasmonic effect of Au and electrocatalytic activity of bimetallic Au and Pt composite.[26] Upon visible laser excitation, the rapid dephasing of free electrons in the nanoparticle leads to the generation of energetic hot electrons and holes. Photogenerated hot holes (h^+) on the surface of NPs accelerate the oxidative chemical transformation of a luminol derivative (L-012). ECL emission at individual NPs proved that the bimetallic NPs showed higher catalytic activity and stability than that of monometallic Au NPs. But lower plasmonic accelerated reaction efficiency was obtained on Au@Pt NPs compared to Au NPs. The precise determination at the individual nanoparticle level mitigates

[a] *State Key Laboratory of Analytical Chemistry for Life Science, School of Chemistry and Chemical Engineering, Nanjing University, Nanjing 210023, P. R. China. E-mail: xujj@nju.edu.cn*
[b] *Institute of Nanochemistry and Nanobiology, School of Environmental and Chemical Engineering, Shanghai University, Shanghai 200444, P. R. China. E-mail: wei_zhao@shu.edu.cn*

† Electronic supplementary information (ESI) available. See DOI: https://doi.org/10.1039/d4cc00001c

‡ These authors contributed equally to this work.

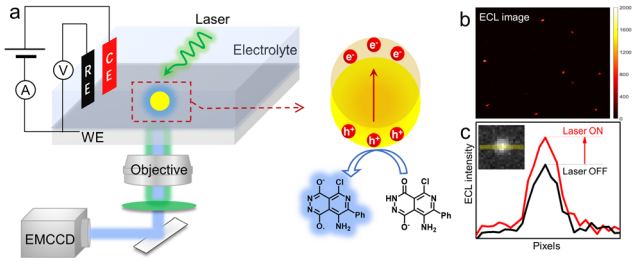

Fig. 1 (a) Schematic illustration of the ECL imaging of hot carriers assisted electrochemical reaction at single Au@Pt NPs (light source: 532 nm). (b) ECL imaging at individual nanoparticles. (c) Image analysis of ECL profile on single nanoparticle with and without laser irradiation.

possible biases from ensemble measurements (Fig. 1b and 1c). This approach shows potential in optimizing the performance of plasmonic nanocatalysts.

Au NPs and Au@Pt NPs were chosen as the subjects to investigate the plasmon-induced electrocatalytic reactions at the single nanoparticle level, leveraging the significant plasmonic effect of Au and superior catalytic activity of Pt.[27] The morphology (Fig. S1a–d, ESI†), optical properties (Fig. S1e and f, ESI†), and ECL emission of L-012 (Fig. S2, ESI†) at Au NPs with diameters of 60 nm, 100 nm, and 200 nm were carefully studied. We finally selected 80 nm Au NPs (Fig. 2a) as the cores, considering both SPR absorption efficiency and ECL intensity. Au@Pt NPs were synthesized by sequentially depositing small Pt particles onto an Au core through the reduction of chloroplatinic acid with 10 mM ascorbic acid in varying amounts. This process resulted in the formation of core–shell nanostructures with average diameters of 90 nm, 100 nm, and 120 nm, respectively (Fig. 2b–d). High-resolution transmission electron microscopy (HRTEM) imaging of a single Au@Pt NP's core–shell interface revealed a 5 nm thick Pt shell with a face-centered cubic (fcc) Au lattice in the core, featuring an Au (111) interlayer spacing of 0.233 nm (Fig. S3a, ESI†). Lattice fringes with a *d*-spacing of 0.222 nm corresponding to the (111) planes of Pt were observed on the small nanoparticles of the Au core. Elemental mapping (Fig. S3b–d, ESI†) confirmed the composition of Au@Pt NPs with varying shell thicknesses. UV-visible spectroscopy analysis of the particles revealed a well-resolved SPR absorption band for 80 nm Au NPs with a center wavelength (λ_{max}) of 552 nm (Fig. 2e and Fig. S1e, ESI†). As Au NPs size increased, the maximum SPR absorption redshifted significantly from 535 nm to 584 nm, consistent with the change in the corresponding scattering band from 568 nm to 634 nm (Fig. S1, ESI†). Pt nanocrystals exhibited a broad absorption throughout the visible range. The growth of Pt layer by layer led to an enlarged SPR absorption and continuous changes in plasmon scattering. After forming a 10 nm Pt shell on the Au core, a broad absorption band was observed with λ_{max} redshifted to 620 nm (Fig. 2f). Distinct SPR scattering was observed on Au NPs and Au@Pt NPs with increased shell thickness under dark-field microscopy (DFM), resulting in an observable change in color from green to orange (Fig. 2g).

First, the conventional potential-triggered ECL emission on individual bimetallic Au@Pt NPs was evaluated by ECLM. Under a pulse potential of 0.6 V *vs.* Ag/AgCl, the plasmonic nanocatalysts catalyzed surrounding luminescent molecules, leading to bright spots in the ECL images (Fig. 3a, d and Fig. S4, ESI†). The L-012–H_2O_2 ECL pathway mechanism is outlined in the ESI.† L-012 oxidation at 0.6 V forms a radical anion ($L^{\bullet -}$), which further reacts with superoxide radical anion ($O_2^{\bullet -}$) to reach the excited state.[26] Comparisons of the ECL intensity of L-012 at individual Au NPs with different diameters revealed that larger particles exhibited stronger ECL emission due to increased surface catalytic sites (Fig. S2, ESI†). The enhanced ECL emission on Au@Pt NPs was attributed not only to increased particle size but also to the superior catalytic activity of platinum compared to gold and synergistic effects from the bimetallic nanoparticles. For instance, 100 nm Au@Pt NPs with Pt shell thickness of 10 nm showed a notable 47.8% increase in

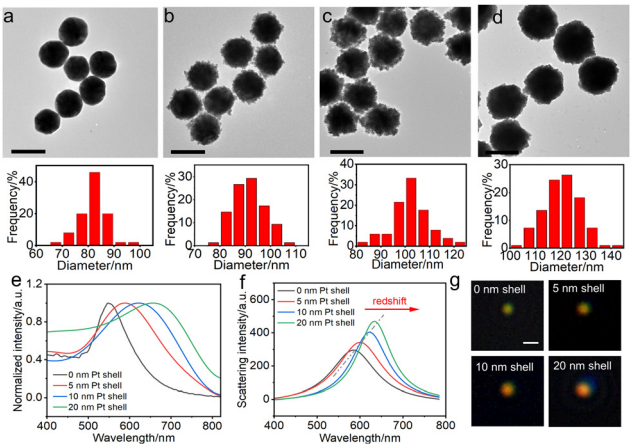

Fig. 2 (a)–(d) Transmission electron microscopy (TEM) images of 80 nm Au NPs and Au@Pt NPs with Pt shell thickness of 5 nm, 10 nm and 20 nm. Inset: Size distribution of the corresponding Au NPs and Au@Pt NPs. Scale bar: 100 nm. (e) SPR absorption spectra, (f) Lorentz-fitted scattering spectra and (g) the corresponding dark-field images of Au NPs and Au@Pt NPs with different Pt shell thicknesses. Scale bar: 2 μm.

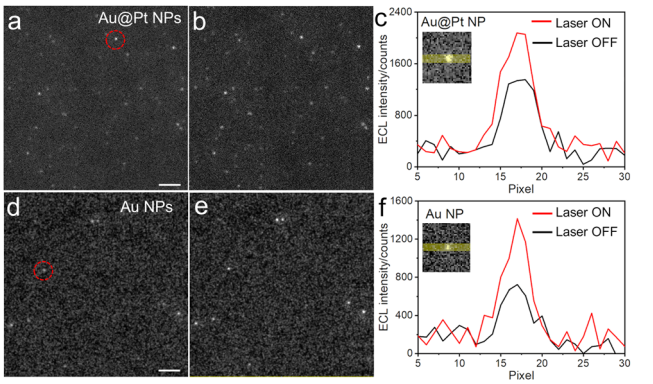

Fig. 3 ECL images of (a) and (b) Au@Pt NPs with a 10 nm Pt shell and (d) and (e) Au NPs before and after illumination of 532 nm CW laser (power density = 172.72 mW cm^{-2}), respectively. Scale bar: 10 μm. (c) and (f) Image analysis of ECL and plasmon-accelerated ECL profile on single Au@Pt NP with a 10 nm Pt shell and Au NP with and without laser irradiation.

ECL intensity, surpassing their 80 nm Au NP counterparts (Fig. S4, ESI†). In contrast, the ECL intensity on 100 nm Au NPs showed 26.3% increase compared to that on 80 nm Au NPs (Fig. S2, ESI†). Importantly, DFM and ECL images showed that Au@Pt NPs exhibited higher electrochemical activity and stability compared to monometallic Au NPs, emphasizing the advantages of bimetallic nanostructures (Fig. S4, ESI†). However, when the Pt shell thickness increased from 10 nm to 20 nm, there was barely any change in ECL intensity. As reported in previous studies,[6,28] bimetallic catalysts have demonstrated superior catalytic performance compared to monometallic counterparts, attributed to the synergistic effect. Given that electrochemical reactions occur at the surface of nanocatalysts, an increase in the Pt shell thickness from 10 nm to 20 nm led to a reduction in exposed Au atoms. This decrease resulted in a diminished synergistic effect and, consequently, a decline in the electrocatalytic activity of the bimetallic nanoparticles. Hence, as the size of nanoparticles increased, there was no concurrent rise in the ECL intensity.

The plasmonic effect induced by nanocatalysts results in the generation of photoexcited hot electrons and hot holes.[18] When a positive potential bias is applied, the hot electrons are driven to transfer to the external circuit. Concurrently, the generated hot holes can persist on the surface of the nanocatalyst, thereby facilitating and accelerating oxidative reactions. Plasmonic-accelerated electrochemical reactions were further investigated using ECLM with a 532 nm continuous wave (CW) laser (Fig. 3). The UV-visible absorption of L-012 below 450 nm and the 465 nm-centered ECL emission peak ensured that the 532 nm laser only stimulated the localized SPR of noble metals, not the fluorescence of L-012 (Fig. S5, ESI†). Laser irradiation was effectively blocked by the utilized filter. As illustrated in Fig. S6b (ESI†), when subjected to 532 nm laser irradiation without any applied potential bias, no emission spots were discernible. This suggests that the localized SPR of Au NPs was impeded, and under such conditions, no other luminescence was detectable. The applied potential of 0.6 V *vs.* Ag/AgCl drove ECL reactions around the particles, evident in ECL bright spots (Fig. S6c, ESI†). Simultaneous laser irradiation and potential bias revealed enhanced ECL emission from individual nanoparticles (Fig. S6d, ESI†). The imaging background slightly increased along with the increasing laser power density (Fig. S7, ESI†). To quantify the plasmon-induced electrochemical reaction, the imaging background was corrected. As displayed in Fig. 3c and f, under a power density of 172.72 mW cm^{-2}, ECL emissions on both Au@Pt NPs and Au NPs significantly improved. Linear sweep voltammetry (LSV) curves (Fig. S8, ESI†) demonstrated that hot carriers around particles assisted electrochemical reactions by increasing oxidation current.

Plasmonic hot carriers, crucial for visible-wavelength photocatalysis, exhibit light intensity-dependent generation.[17,29] The ECL intensity dependence on the laser power density was investigated using Au@Pt NPs with a 10 nm shell thickness. Increasing the power density of the 532 nm laser from 106.72 to 172.72 mW cm^{-2} resulted in brighter ECL emission from individual Au@Pt NPs (Fig. 4). The ΔECL ratio, calculated by the percentage increase in ECL intensity before and after

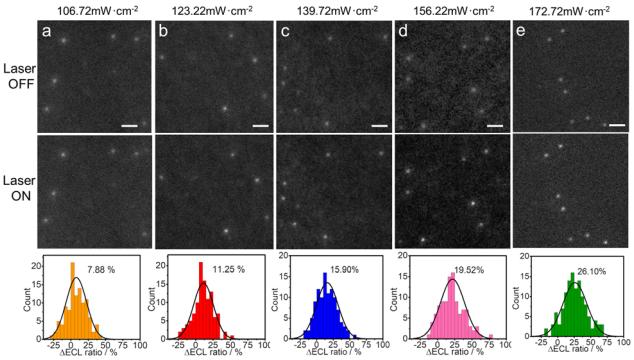

Fig. 4 Top: ECL images of individual Au@Pt NPs with a 10 nm Pt shell with and without 532 nm laser irradiation with power density of (a) 106.72 mW cm^{-2}, (b) 123.22 mW cm^{-2}, (c) 139.72 mW cm^{-2}, (d) 156.22 mW cm^{-2}, and (e) 172.72 mW cm^{-2}. Scale bar: 5 μm. Bottom: Corresponding statistical analysis of the distributions of ECL intensities at individual Au@Pt NPs with a 10 nm Pt shell under laser irradiation with different power densities.

photoexcitation *via* background correction, revealed a rise from 7.88% to 26.10% based on the analysis of 120 spots. This value signifies the occurrence of plasmon-induced electrochemical reactions. It should be noted that the laser irradiation measurements were conducted subsequent to conventional ECL measurements. Due to potential influences from surface contamination and oxidation, a subset of the nanoparticles exhibited a slight decrease in ECL intensity during these measurements. Statistical analysis of ECL intensity on individual Au@Pt NPs displayed a linear relationship with power density (Fig. S9a, ESI†). Similar measurements on Au NPs modified ITO indicated a comparable increasing trend in ECL intensity on individual Au NPs (Fig. S9b, ESI†). Despite the lower ECL signal intensity on individual Au NPs compared to Au@Pt NPs, the percentage increase under laser irradiation was higher, rising from 13.29% to 44.41% as the power density increased from 106.72 to 172.72 mW cm^{-2}.

The plasmon-induced photoelectrochemical conversion efficiency hinges on the generation, recombination, and oxidation reaction efficiency of hot electron–hole pairs.[30] Bimetallic nanoparticles, evidenced by faradaic current and ECL imaging, demonstrate heightened catalytic activity for the charge transfer reaction of L-012. The decline in photocatalytic efficiency is attributed to a reduced abundance of hot holes on the particle surface, resulting from two factors. Firstly, at the investigated excitation wavelength of 532 nm, the dominance of the inter-band transition of Au contributes significantly, with the Pt shell acting as an impediment to the absorption efficiency of Au. Secondly, the growth of the Pt shell extends the effective path length of hot carriers toward the surface, consequently leading to an increase in the recombination of hot electrons and holes.

To assess the impact of hot carriers' path length, we conducted a systematic investigation of plasmon-induced ECL on Au@Pt NPs with varying shell thicknesses, ranging from 5 nm to 20 nm. (Fig. 5a and Fig. S10 and S11, ESI†). ΔECL ratios on both Au@Pt NPs and Au NPs linearly correlate with laser power density (Fig. 5b). Increasing Pt layer thickness results in a noticeable reduction in the slope of ΔECL, particularly evident in the transition from a 10 nm to a 20 nm Pt shell thickness,

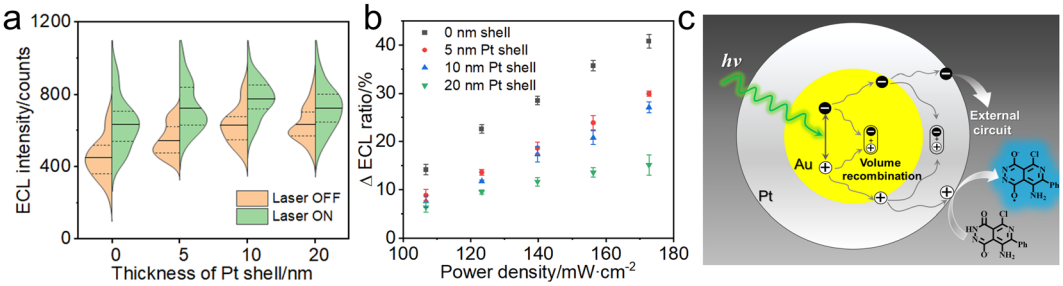

Fig. 5 (a) Statistical distribution of ECL intensity of Au NPs and Au@Pt NPs with different Pt shell thicknesses with laser OFF and ON at the 172.72 mW cm^{-2} (n = 50). (b) The increased ECL intensity ratio on Au@Pt NPs with different Pt shell thicknesses and Au NPs as a function of laser power density. (c) Schematic illustration of plasmon-induced hot carriers generation and recombination, and hot holes driven oxidation reaction.

signifying a substantial influence on the transfer of electron–hole pairs generated by laser irradiation. As illustrated in Fig. 5c, the interaction between photoexcited hot electrons and hot holes involves both volume recombination and surface recombination. Applying bias and oxidative reactions can enhance the separation efficiency. However, with the progressive thickening of the Pt shell, it introduces a longer diffusion distance for hot carriers, increasing the likelihood of non-radiative decay and subsequent recombination. Consequently, bimetallic nanostructures with a Pt shell demonstrate lower plasmonic accelerated reaction efficiency compared to monometallic Au NPs, attributed to a decrease in the abundance of hot holes available for oxidative reactions.

In summary, this study introduces a novel methodology employing ECLM to explore plasmon-induced electrochemical reactions at the individual nanoparticle scale. We synthesized plasmonic Au@Pt core–shell NPs with varying Pt shell thicknesses and compared their performance with pure Au NPs through extensive ECLM analysis. Under 532 nm laser irradiation, this study revealed lower plasmonic accelerated reaction efficiency for the bimetallic core–shell NPs compared to that of monometallic Au NPs. This disparity is attributed to diminished absorption efficiency and an extended transfer path for hot carriers. The quantifiable enhancement in ECL intensity serves as a reliable metric for the assessment of plasmon-induced electrochemical reactions. ECLM proves to be an intuitive technology for observing these phenomena at the individual nanocatalyst level, mitigating potential biases from ensemble measurements. The demonstrated correlation between ECL intensity and laser power density underscores the importance of understanding the plasmonic effect and optimizing the performance of plasmonic nanocatalysts across various applications, such as energy conversion and storage, photocatalysis, and sensing.

This work was supported by the National Natural Science Foundation (Grants 22034003, 22374095 and 22074063) of China.

Conflicts of interest

The authors declare no competing financial interest.

Notes and references

1 M. L. Brongersma, N. J. Halas and P. Nordlander, *Nat. Nanotechnol.*, 2015, **10**, 25–34.
2 T. Ding, J. Mertens and A. Lombardi, *et al.*, *ACS Photonics*, 2017, **4**, 1453–1458.
3 M. Wang, M. Ye and J. Iocozzia, *et al.*, *Adv. Sci.*, 2016, **3**, 1600024.
4 W. Zhang, J. Li and X. H. Xia, *et al.*, *Angew. Chem., Int. Ed.*, 2022, **61**, e202115819.
5 Y. Zhang, S. He and W. Guo, *et al.*, *Chem. Rev.*, 2018, **118**, 2927–2954.
6 C. Xia, W. He and X. F. Yang, *et al.*, *Anal. Chem.*, 2022, **94**, 13440–13446.
7 M. Vadai, D. K. Angell and F. Hayee, *et al.*, *Nat. Commun.*, 2018, **9**, 4658.
8 S. Mukherjee, F. Libisch and N. Large, *et al.*, *Nano Lett.*, 2013, **13**, 240–247.
9 S. Linic, P. Christopher and D. B. Ingram, *Nat. Mater.*, 2011, **10**, 911–921.
10 A. E. Schlather, A. Manjavacas and A. Lauchner, *et al.*, *J. Phys. Chem. Lett.*, 2017, **8**, 2060–2067.
11 Z. Zheng, W. Xie and M. Li, *et al.*, *Nano Energy*, 2017, **41**, 233–242.
12 X. Guo, X. Li and S. Kou, *et al.*, *J. Mater. Chem. A*, 2018, **6**, 7364–7369.
13 H. X. Zhang, Y. Li and M. Y. Li, *et al.*, *Nanoscale*, 2018, **10**, 2236–2241.
14 F. Shi, J. He and B. Zhang, *et al.*, *Nano Lett.*, 2019, **19**, 1371–1378.
15 J. Zhao, S. Xue and R. Ji, *et al.*, *Chem. Soc. Rev.*, 2021, **50**, 12070–12097.
16 C. Wang, X. G. Nie and Y. Shi, *et al.*, *ACS Nano*, 2017, **11**, 5897–5905.
17 E. Pensa, J. Gargiulo and A. Lauri, *et al.*, *Nano Lett.*, 2019, **19**, 1867–1874.
18 C. P. Byers, B. S. Hoener and W. S. Chang, *et al.*, *J. Phys. Chem. B*, 2014, **118**, 14047–14055.
19 Y. Yu, V. Sundaresan and K. A. Willets, *J. Phys. Chem. C*, 2018, **122**, 5040–5048.
20 W. Li, J. Miao and T. Peng, *et al.*, *Nano Lett.*, 2020, **20**, 2507–2513.
21 X. Mao, C. Liu and M. Hesari, *et al.*, *Nat. Chem.*, 2019, **11**, 687–694.
22 C. Ma, W. Wu and L. Li, *et al.*, *Chem. Sci.*, 2018, **9**, 6167–6175.
23 M. M. Chen, W. Zhao and M. J. Zhu, *et al.*, *Chem. Sci.*, 2019, **10**, 4141–4147.
24 M. M. Chen, C. H. Xu and W. Zhao, *et al.*, *J. Am. Chem. Soc.*, 2021, **143**, 18511–18518.
25 W. Zhao and J. J. Xu, *Chin. J. Chem.*, 2022, **40**, 1975–1986.
26 Z. Xi, H. Lv and D. P. Erdosy, *et al.*, *Nanoscale*, 2017, **9**, 7745–7749.
27 M. J. Zhu, J. B. Pan and Z. Q. Wu, *et al.*, *Angew. Chem., Int. Ed.*, 2018, **57**, 4010–4014.
28 J. Shen, S. Xu and C. Zhao, *et al.*, *ACS Appl. Mater. Interfaces*, 2021, **13**, 57597–57608.
29 A. Al-Zubeidi, B. S. Hoener and S. S. E. Collins, *et al.*, *Nano Lett.*, 2019, **19**, 1301–1306.
30 J.-W. Xue, C.-H. Xu and W. Zhao, *et al.*, *Nano Lett.*, 2023, **23**, 4572–4578.